

Article

Tropical Cyclone Rainfall Estimates from FY-3B MWRI Brightness Temperatures Using the WS Algorithm

Ruanyu Zhang ^{1,2} , Zhenzhan Wang ^{1,*} and Kyle A. Hilburn ³

¹ Key Laboratory of Microwave Remote Sensing, National Space Science Center, Chinese Academy of Sciences, Beijing 100190, China; ruanyu_zhang@163.com (R.Z.); wangzhenzhan@mirslab.cn (Z.W.)

² University of Chinese Academy of Sciences, Beijing 100049, China

³ Cooperative Institute for Research in the Atmosphere, Colorado State University, Fort Collins, CO 80523, USA; kyle.hilburn@colostate.edu

* Correspondence: wangzhenzhan@mirslab.cn; Tel.: +86-10-6258-6454

Received: 24 September 2018; Accepted: 5 November 2018; Published: 8 November 2018



Abstract: A rainfall retrieval algorithm for tropical cyclones (TCs) using 18.7 and 36.5 GHz of vertically and horizontally polarized brightness temperatures (Tbs) from the Microwave Radiation Imager (MWRI) is presented. The beamfilling effect is corrected based on ratios of the retrieved liquid water absorption and theoretical Mie absorption coefficients at 18.7 and 36.5 GHz. To assess the performance of this algorithm, MWRI measurements are matched with the National Snow and Ice Data Center (NSIDC) precipitation for six TCs. The comparison between MWRI and NSIDC rain rates is relatively encouraging, with a mean bias of -0.14 mm/h and an overall root-mean-square error (RMSE) of 1.99 mm/h. A comparison of pixel-to-pixel retrievals shows that MWRI retrievals are constrained to reasonable levels for most rain categories, with a minimum error of -1.1% in the 10–15 mm/h category; however, with maximum errors around -22% at the lowest (0–0.5 mm/h) and highest rain rates (25–30 mm/h). Additionally, Advanced Microwave Scanning Radiometer for Earth Observing System (AMSR-E) Tbs are applied to retrieve rain rates to assess the sensitivity of this algorithm, with a mean bias and RMSE of 0.90 mm/h and 3.11 mm/h, respectively. For the case study of TC Maon (2011), MWRI retrievals underestimate rain rates over 6 mm/h and overestimate rain rates below 6 mm/h compared with Precipitation Radar (PR) observations on storm scales. The Tropical Rainfall Measuring Mission (TRMM) Microwave Imager (TMI) rainfall data provided by the Remote Sensing Systems (RSS) are applied to assess the representation of mesoscale structures in intense TCs, and they show good consistency with MWRI retrievals.

Keywords: tropical cyclone; rain rate; precipitation; remote sensing; radiometer; retrieval algorithm

1. Introduction

Tropical cyclones (TCs) are high-impact meteorological phenomena accompanied by high winds, torrential precipitation, and storm surges, and occur in nearly every ocean basin in the Northern Hemisphere every year, which not only has a dramatic impact on coastal and inland regions, but also brings catastrophic impacts to human life, property, and ecology [1–3]. Hence, improving TC forecasts is an important field of study. Tropical precipitating cloud systems are one of the most important elements in the global climate system [4]. Globally, precipitation measurements did not become available until the era of satellite Earth observations which employ infrared and microwave radiometric techniques [5]. The advantage of microwave frequency is that microwaves penetrate or “see through” clouds with little attenuation and give an uninterrupted observation down to the sea surface during

the day and night [6]. This is a distinct advantage over space-borne infrared and optical measurements that are obstructed by clouds due to their shorter wavelengths than microwaves [7]. Hence, passive microwave remote sensing plays a key role in providing vital information for understanding and studying global weather and climate changes. Since most of the large range of TCs often occurs over oceans, TC rain rates are difficult to quantify based on ground-based instruments such as rain gauges and radars. Even if coastal precipitation measurements are detected by rain gauges, they do not adequately detect and measure the structure and rain rate of TCs over oceans or their surrounding environment. The surface radar datasets have a limited spatial extent [8]. Consequently, satellite-derived measurements are frequently used to detect Earth system processes and parameters, especially to monitor the tracks of TCs. Although satellite observations have relatively large random errors at small scales, their global nature makes them suitable for addressing potential changes in global precipitation extremes [9].

Passive microwave radiometers onboard low-Earth orbiting satellites are able to quickly cover the globe, providing approximately two overpasses per day at a given location [10]. Radiometers have been widely applied to global observations and measurements of Earth system processes and parameters, especially monitoring TCs' development and characterizing mesoscale structures. The first passive microwave instrument in orbit dates back to the mid-1960s [11]. The first Special Sensor Microwave Imager (SSM/I) aboard the Defense Meteorological Satellite Program (DMSP) was launched successfully in 1987 [12], making it possible to provide measurements of atmospheric moisture and global surface precipitation [13]. The Microwave Imager (TMI) and Precipitation Radar (PR) onboard the Tropical Rainfall Measuring Mission (TRMM) satellite began operating in 1997 to provide detailed satellite measurements between 40°N and 40°S [14]. Based on the success of TRMM, the Global Precipitation Measurement (GPM) core instruments Microwave Imager (GMI) and dual-frequency Precipitation Radar (DPR) provide improved capabilities of precipitation measurements [15]. Blended products of global rainfall measurements are available at 30 min of temporal resolution across the globe [16]. The Advanced Microwave Scanning Radiometer for Earth Observing System (AMSR-E) was on board the National Aeronautics and Space Administration (NASA) Aqua satellite working from 2002 to 2011 [17]. The Microwave Radiation Imager (MWRI), the first space-borne microwave sensor in China, began operating in 2010 [18].

The concept, using satellite microwave observations to retrieve accurate oceanic precipitation rates, was first proposed by [19]. With the rapid development of satellite-based instruments, a variety of models and algorithms for retrieving precipitation rates based on microwave remote sensing have been developed and have evolved to extract information from passive microwave radiometer measurements [8]. These precipitation retrieval algorithms are generally classified into two schemes: empirical and physically based schemes. The empirical models are generally based on the simple empirical relationship between the brightness temperature (T_b) observed by radiometers and rain rates detected by conventional instruments, such as scatter methods [20,21], and polarization-corrected temperature (PCT) [22,23]. However, empirical approaches are difficult to extend to global regions, while physical methods generally provide more precipitation parameters, such as vertical profiles of precipitation and hydrometeor types [8,24]. Over the ocean, physical methods have been developed to retrieve rain rates for SSM/I, TMI, GMI, AMSR, AMSR-E, and the Advanced Microwave Scanning Radiometer 2 (AMSR2) [13,25–29], using the relationship between T_b s and rain rate. However, there are few studies based on MWRI observations [30,31].

Over the past 20 years, TC studies based on radiometers have mainly focused on three aspects: TC best-track databases [32], meteorological characteristics of TCs [33], and rainfall retrievals of TCs [24,34]. In surface rainfall retrieval algorithms, however, deficiencies have been shown when compared with estimates of radar and TMI precipitation observations, with an underestimation of inner-core and high rain rate regions of TCs [34]. MWRI T_b s observations have not yet been thoroughly utilized in detecting surface precipitation rates in TCs, while the rainfall and hydrometeor profiles have been retrieved based on the Goddard profiling (GPROF [35]) algorithm [30]. Therefore,

the purpose of this paper is to find a suitable methodology for MWRI observations to estimate the surface rain intensities of TCs over oceans. For accurate radiometer retrievals of surface rain rates, methods combining different frequencies have been used. A physical method is developed to retrieve surface rain rate using vertically and horizontally polarized Tbs provided by the SSM/I, AMSR and AMSR-E instruments [7,13,25], which ignores precipitation scattering effects and only considers the emission effects on measurements. However, these algorithms mainly focus on global precipitation estimates. In an attempt to demonstrate the rainfall retrieval capability of TCs utilizing measurements of microwave radiometers, it is necessary to do more studies on MWRI observations.

This paper advances the effort to estimate surface rain rates of TCs based on the Wentz and Spencer (hereafter, WS) physical algorithm [13] using FY-3B MWRI 18.7 and 36.5 GHz vertically and horizontally polarized Tb measurements. A brief description of MWRI channel characteristics is given in Section 2. Section 3 introduces all the datasets used in this paper, including MWRI Tbs, AMSR-E Tbs, the Global Forecast System (GFS) environmental product, the National Snow and Ice Data Center (NSIDC) rainfall product, and the TRMM rainfall products. The algorithm scheme for surface rainfall retrievals using MWRI Tbs is described in Section 4. Detailed results of the MWRI WS algorithm are provided and evaluated in Section 5, including the case study of TC Maon (2011). Section 5 also presents mesoscale structure comparisons of select TCs. Section 6 provides a discussion of the results. Finally, Section 7 draws conclusions based on our results.

2. Instrument Description

The Feng-Yun 3B (FY-3B), a Chinese second-generation afternoon-configured polar-orbiting satellite, travels 14.17 orbits over 24 h and crosses the equator in ascending modes at 1:40 P.M. local time with a revisit period of 6 days [36]. The MWRI instrument on board the FY-3B satellite conically scans the Earth with a swath width of 1400 km and a viewing angle of 45° [18]. It is a total power passive radiometer that has five frequencies at 10.65, 18.7, 23.8, 36.5, and 89.0 GHz, and each frequency has vertical (V) and horizontal (H) polarizations.

The channel configuration and viewing geometry of MWRI are very similar to the existing microwave imagers, such as AMSR-E, SSM/I and TMI, which provide comparable measurements and products as MWRI retrievals. The instrument performance requirements of MWRI are provided in Table 1. Since MWRI's launch, the sensor has been operating with high stability, providing continuous observations. MWRI collects observations under different weather conditions during the day and night to monitor total precipitation water (TPW), cloud liquid water, surface rain, snow–water equivalent, sea surface temperature (SST), wind speed, and sea ice constant. These parameters are helpful for improving the accuracy of weather forecasting and for TC monitoring.

Table 1. The main specifications of the FY-3B Microwave Radiation Imager (MWRI) [36].

Frequency (GHz)	10.65	18.7	23.8	36.5	89.0
Polarization	V/H	V/H	V/H	V/H	V/H
Resolution (km)	51 × 85	30 × 50	27 × 45	18 × 30	9 × 15
Sensitivity (K)	0.5	0.5	0.5	0.5	0.8
Calibration error (K)	1.5	1.5	1.5	1.5	1.5
Swath width	1400 km				
Scan mode	Conical scanning				
Scan cycle	1.8 s				
Viewing angle	45°				
Samples	254				
Sampling interval	2.08 ms				

3. Datasets and Processing

This study employs the MWRI Tbs, the AMSR-E Tbs, the NSIDC rain rates, the PR surface rain rates, and the Remote Sensing Systems (RSS) TMI rainfall product to explore the accuracy and

mesoscale structures of MWRI rainfall retrievals for six selected TCs. The domain is limited to the western North Pacific Ocean (5°N–50°N, 100°E–175°E) to form a geographically well-understood test bed. The GFS is used to provide environmental parameters, such as SST, TPW, and wind speed for this rainfall retrieval algorithm. The NSIDC rainfall product and the TRMM precipitation data serve as the evaluation reference and a priori surface rain rates. Additionally, the AMSR-E Tb dataset provided by the NSIDC is used to retrieve rain rates for the same selected TCs which will be compared with MWRI retrievals.

3.1. Brightness Temperature

The Tbs used in the WS algorithm are the FY-3B level-1 MWRI products provided by the National Satellite Meteorological Center Feng Yun Satellite Data Center (<http://satellite.nsmc.org.cn/Portal-Site/default.aspx>). Yang et al. [18] developed a unique calibration system designed with a main reflector viewing both cold and hot calibration targets for the MWRI system. The calibration targets and the Earth scene are all viewed by the same main reflector, and the calibration is proven to work well. As shown in Table 1, MWRI has five frequencies varying from 10.65 to 89 GHz, and the absolute calibration errors are 1.5 K for all frequencies. The details of the calibration approach and accuracy evaluation are described in [18]. During each scan, each channel consists of different locations and resolution. The sensitivity of Tbs at different channels varies with atmospheric and surface geophysical parameters [36]. MWRI includes a 6.9 GHz frequency, and its poor spatial resolution will limit the usefulness for rainfall retrievals [29]. Therefore, the 18.7 and 36.5 GHz Tbs (hereafter, 19 and 37 GHz) are chosen for rainfall retrievals in the MWRI WS algorithm, which are more sensitive to precipitation.

The AMSR-E instrument is a conical scanning passive microwave radiometer, which provides measurements for 12 channels (6.9 V/H, 10.79 V/H, 18.79 V/H, 23.89 V/H, 36.59 V/H, 89.09 V/H GHz) over the globe [17]. Because MWRI and AMSR-E have the same local ascending/descending times, similar channels, and view geometries, AMSR-E Tbs are collected to evaluate the sensitivity of the MWRI WS algorithm. The AMSR-E Tbs are provided by the AMSR-E/Aqua L2A Global Swath Spatially-Resampled Tbs (Version 3), which are downloaded from the NSIDC website (http://nsidc.org/data/AE_L2A).

3.2. GFS Environmental Product

To provide input parameters for this algorithm, the GFS forecast data are used as an a priori dataset produced by the National Centers for Environmental Prediction (NCEP) (<https://www.ncep-c.noaa.gov/data-access/model-data/model-datasets/global-forecast-system-gfs>). The entire globe is covered by the GFS at a horizontal resolution of 1 degree in latitude and longitude. It is particularly suitable for the algorithm requirements and provides high-precision environmental parameters, especially wind speed, TPW, and SST measurements at the time of satellite overpasses.

3.3. NSIDC Rainfall Product

The AMSR-E/Aqua Level-2B precipitation product (Version 3) provided by the NSIDC (https://nsidc.org/data/AE_Rain) is used as the reference dataset and applied for evaluating the accuracy of the retrieved rain rate. In each satellite orbit, the AMSR-E/Aqua Level-2B precipitation provides high-quality instantaneous surface rain rates over land and oceans with a 5 km spatial resolution along the scan and 10 km spatial resolution along the track. The precipitation dataset is generated from the GPROF2010 (Version 2) [28] using the AMSR-E Level-2A Tbs (Version 3). The GPROF2010 is a Bayesian retrieval scheme that is developed for TRMM TMI by Kummerow et al. [28]. The GPROF rainfall results compare well with atoll gauge data over oceans and the Global Precipitation Climatology Centre (GPCC) gauge network over land [26]. Therefore, the GPROF has been finalized for AMSR-E. Wolff and Fisher [37] have assessed the performance of 4-year (2003–2006) AMSR-E GPROF retrievals using ground-based rain estimates from TRMM ground validation sites, which shows the AMSR-E estimates exhibit the highest correlation (0.83) and a low error (−5.3%) over oceans. The AMSR-E retrievals

have also been investigated in correspondence with the radar-based convective and stratiform rain indexing [38]. Due to the similar local time of ascending nodes (LTAN) of AMSR-E and MWRI (13:30 and 13:40, respectively), the NSIDC rainfall product is a good candidate for the comparison with MWRI rainfall retrievals.

3.4. TRMM Precipitation Data

The TRMM satellite was launched on 27 November 1997, carrying five instruments, two of which are the TMI and PR. The TMI is a multi-channel, dual polarized, conical scanning passive microwave radiometer capable of quantifying not only surface rain rate but also SST, sea surface wind speed, columnar water vapor, and cloud liquid water [14]. In this study, the TMI rainfall data provided by RSS (<http://www.remss.com/missions/tmi/>) are used as a reference dataset to present the mesoscale of selected TCs. The TMI orbital data mapped to 0.25° grid covering the globe and divided into two maps based on ascending and descending passes.

The PR instrument is a Ku-band radar operating at 13.8 GHz with a field of view (FOV) of approximately 5 km. The Ku-band radar has a swath of approximately 250 km, and it provides vertical sampling with a vertical resolution of 250 m from ground level up to 20 km [39]. The PR offers vertical profiles of precipitation in global tropic regions based on the time delay of precipitation-backscattered return power [40]. The standard TRMM PR 2A25 product (Version 7) obtained from the NASA Precipitation Measurement Missions (PPS) (<https://pmm.nasa.gov/>) provides the attenuation-corrected radar reflectivity profile, freezing level estimate, and near-surface rain rate, which is used to evaluate MWRI rainfall retrievals. The evaluation analysis of near-surface rain rate estimates from PR 2A25 product, Japanese high-temporal-resolution rain gauge dataset, and the National Oceanic and Atmospheric Administration/National Severe Storms Laboratory (NOAA/NSSL)'s ground-based radar dataset shows that the near-surface rain rate in Version 7 is generally reliable and has been improved largely compared with PR 2A25 Version 6 [41,42]. The detailed information of validation is described in [41,42].

3.5. Data Matchup

To evaluate the rain retrievals of TCs, MWRI measurements coincident with the NSIDC rainfall product are collected. This paper mainly focuses on the TCs occurring over the western North Pacific Ocean, which generally affects the spatial distribution of regional precipitation in China [43]. MWRI observations for six selected TCs during 2011 are collected: Songda in May, Maon in July, Mufia in August, Talas in August, Sonca in September, and Nesat in September. The TC dataset, termed as best-track data, consists of the best estimates of storm position and intensity at 6-h intervals only. The best-track data are a result of postseason reanalysis of a storm's position and intensity from all available data, such as the ship, surface, and satellite observations [32]. Figure 1 depicts the corresponding intensity and best-track analysis data of the six selected TCs, which are obtained from the Joint Typhoon Warning Center (JTWC) (<http://www.metoc.navy.mil/jtwc/jtwc.html?best-tracks>).

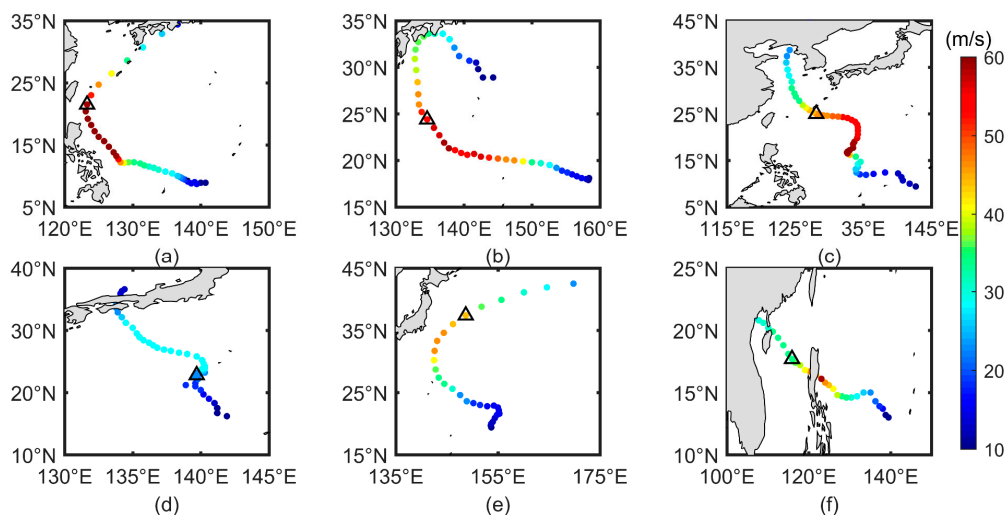


Figure 1. Corresponding intensity and best-track locations of the six selected tropical cyclones (TCs): (a) Songda, 20 to 29 May; (b) Maon, 11 to 2 July; (c) Mufia, 25 July to 8 August; (d) Talas, 25 August to 4 September; (e) Sonca, 14 to 20 September; (f) Nesat, 23 to 30 September. The triangle area in each TC is the target area for analysis.

The time of matching MWRI observations and NSIDC rain rates is within 30 min. Within the 30-min time interval between these two products, a TC does not move a relatively large distance and its overall distribution of precipitation does not undergo significant changes. All the NSIDC points within a 5 km radius of each MWRI pixel are selected for data matchup, in which the closest point with this MWRI pixel will be picked and used as the best-matched point. The NSIDC rainfall product is based on AMSR-E rainfall retrievals developed by the GPROF2010 algorithm [28], and it performs at a high resolution, approximately 5 km \times 10 km, which is around the size of the AMSR-E 89 GHz FOV. Therefore, the NSIDC rainfall product is resampled to make it comparable to MWRI retrievals at the 37 GHz footprint. Using the nearest neighbor interpolation, all NSIDC rainfall points within a radius of 23 km (around the size of MWRI 37 GHz, 18 km \times 30 km) are selected and then averaged with a weighting inversely proportional to distance. The total number of matched retrieved rain rates and NSIDC rainfall data is 101,879, which is used for rain retrieval intercomparison. Table 2 shows the statistics of the six selected TCs in the datasets, which includes the TC's name, date, the maximum wind speed, and the matched points of each TC.

Table 2. Statistics of the six selected TCs: TC's name, MWRI observation date, and the matched point number of MWRI and Advanced Microwave Scanning Radiometer for Earth Observing System (AMSR-E) observations.

TC's Name	Date	Matched Point Number
Songda	17:25, 27 May 2011	18,263
Maon	03:53, 17 July 2011	19,234
Mufia	17:21, 4 August 2011	15,153
Talas	04:19, 27 August 2011	14,095
Sonca	16:07, 19 September 2011	21,852
Nesat	05:53, 28 September 2011	13,282
Total number of matched pixels: 101,879		

Since the TRMM PR FOV is approximately 5 km, the spatial and temporal intervals for the collocation between MWRI rain retrievals and TRMM PR rain rates are same as the method of NSIDC product. However, there is only one TC coincident with both MWRI and PR observations due to the narrow swath of PR and the different equatorial crossing times of PR and MWRI.

4. Methodology

4.1. Microwave Radiation

The Tbs observed by a satellite radiometer depend on a number of sea surface and atmospheric geophysical variables, as well as measurement geometry, which has been used to estimate various environmental parameters, such as precipitation rate, SST, and wind speed [13,25,27,28,44,45]. Tbs at the top of atmosphere measured by a satellite radiometer are expressed as the sum of upwelling atmospheric radiation (T_{UP}), the sea surface direct emission attenuated by the intervening atmosphere, the down-welling atmospheric radiation (T_{DN}) reflected upward by sea surface, and the reflected cosmic background radiation (T_{CO}) [46]. The basic form of the radiation transfer equation for the microwave band is expressed as follows:

$$T_b = T_{UP} + \tau[ET_s + (1 - E)(\Omega T_{DN} + \tau T_{CO})], \quad (1)$$

where E is the sea surface emissivity, T_s is the SST, and τ is the transmittance through the atmosphere. The Ω accounts for non-specular reflection from the rough sea surface. The cosmic background radiation temperature T_{CO} is approximately 2.7 K. Figure 2 shows the Tbs received by a radiometer.

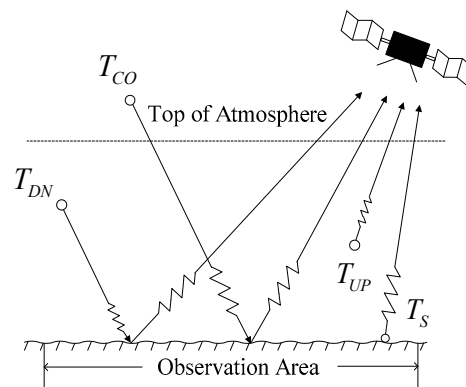


Figure 2. The Tbs measured by a radiometer.

4.2. Retrieval Algorithm

Previous studies have developed rainfall retrieval algorithms for SSM/I [13], TMI [26], and AMSR-E [29]. The study of the WS algorithm focused on 19 and 37 GHz H and V polarization data from SSM/I to retrieve global rain rates. An improved algorithm, the unified microwave ocean retrieval algorithm (UMORA) developed by [25], has been applied to SSM/I, TMI, GMI, AMSR-E, AMSR2, and WindSat. However, there are few studies focusing on rainfall retrievals inside TCs based on MWRI Tbs. Consequently, based on the WS algorithm, an algorithm for retrieving rain rates inside TCs by using MWRI 19 and 37 GHz Tbs is proposed. Since the upwelling radiation at higher frequencies is strongly affected by ice scattering, the retrieval uses lower frequencies where radiation is absorbed and re-emitted by liquid hydrometeors to obtain the information of the column-integrated liquid water [47]. High rain intensities not only change the atmospheric attenuation but also influence the sea surface dielectric properties in a complicated manner [48]. The emissivity over the ocean is approximately from 0.4 to 0.5, and this low surface emissivity ensures a strong contrast between a radiometrically cold and warm background and the precipitation-related atmospheric signature [21,26]. Since the background radiometric signal over the ocean is low, the additional emissions from the precipitation and polarization signature are utilized to identify rain intensity using low-frequency channels (10 to 37 GHz) [10].

One of the key steps of rainfall retrieval is relating the Tbs to rain rates based on Equation (1). Generally, three processes should be taken into account: absorption, emission, and scattering. The atmospheric absorption includes three components: water vapor, oxygen, and liquid water

in the form of clouds or rain rates [46]. Raindrops increase the attenuation of the atmosphere at high radar frequencies [48], and it should be noted that the scattering induced by raindrops can be ignored for frequencies below 10 GHz when the rain intensity is less than 12 mm/h [49]. Because Equation (1) obscures the essential physics of rain retrieval, a simplified form of Equation (1) is necessary. Two assumptions are made: (1) we ignore the cosmic microwave background and small effects of non-specular reflection; and (2) we assume that the ocean–atmosphere system is isothermal with the effective temperature (T_E). In this algorithm, dual-polarization Tb measurements are used to separate emission signals from scattering signals. Based on the radiation transfer equation in Equation (1), a highly simplified model for Tb is obtained following [13]:

$$T_B = T_E(\tau) \left(1 - \tau^2 \rho_P\right), \quad (2)$$

where ρ_P is the reflectivity of the sea surface of different polarizations, P (V and H). Despite its simplicity, Equation (2) is still a good approximation to the Tb s model function. A two-way transmittance is given by

$$\tau^2 = \frac{T_{BV} - T_{BH}}{\rho_H T_{BV} - \rho_V T_{BH}}. \quad (3)$$

Using dual-polarization observations from MWRI 19 or 37 GHz Tb s, the T_E term is eliminated and τ_{19}^2 or τ_{37}^2 is separated from T_E . Hence, the accurate liquid water absorption A_{L19} and A_{L37} are obtained through the two-way transmittance τ_{19}^2 and τ_{37}^2 , respectively. Additionally, the total atmosphere transmittance is given by

$$\tau = \exp[-\sec\theta(A_O + A_V + A_L)], \quad (4)$$

where A_O , A_V , and A_L are oxygen, water vapor, and liquid water absorption, respectively. θ is the incident angle of the MWRI instrument. A_O and A_V are given by [46] as functions of effective air temperature and columnar water vapor. The footprint-averaged attenuation A_L is

$$A_L = \int A' P(A') dA', \quad (5)$$

where $P(A')$ is the probability distribution function for attenuation within the footprint. Then, the footprint-averaged two-way transmittance is given by

$$\tau_L^2 = \int \exp(-2A' \sec\theta) P(A') dA'. \quad (6)$$

If the beamfilling were uniform, $P(A')$ would be the delta function, and integrating (6) yields

$$\tau_L = \exp(-\sec\theta \cdot A_L), \quad (7)$$

and this is inverted to provide the total liquid water (cloud and rain water) absorption A_L :

$$A_L = -\ln(\tau_L) / \sec\theta. \quad (8)$$

Because the nonlinear relationship between rain rate and Tb occurs when averaging over the radiometer footprint, there is a systematic underestimation of total liquid water absorption, which is referred to as the “beamfilling effect”. The WS algorithm shows that if the sub-pixel absorption follows an exponential distribution, the relationship between the absorption A_L within the radiometer footprint and the true mean value \hat{A}_L is given by

$$\hat{A}_L = \frac{e^{2A_L \beta^2 \sec\theta} - 1}{2\beta^2 \sec\theta}, \quad (9)$$

where A_L and \hat{A}_L represent liquid water absorption before and after beamfilling correction, respectively. β is the normalized RMSE variation for the cloud and rain water absorption A_L , which is related to the variability of liquid water in footprint and is independent of frequency.

The ratio A_{L37}/A_{L19} is less than that predicted by the theoretical Mie absorption ratio when the beamfilling effect is significant. When $A_{L37}/A_{L19} \geq \hat{A}_{L37}/\hat{A}_{L19}$, the beamfilling effect is not significant and no beamfilling correction is performed ($\beta = 0$). The theoretical Mie absorption ratio varies from 3.5 for light absorption to 2.8 for heavy absorption values. The beamfilling correction is made by finding a β value that yields the ratio $\hat{A}_{L37}/\hat{A}_{L19}$ close to the given Mie theory ratio with a monotonically increasing value of β from 0 to 1. The maximum value of the exponent $2A_{L37}\beta^2 \sec \theta$ in Equation (9) is capped at 3.0. Additionally, the maximum values of \hat{A}_{L19} and \hat{A}_{L37} are not allowed to exceed 1.2, which correspond to observations of the heavy rain rate that the 37 and 19 GHz Tbs have saturated. The effect of these limits is to place a rain rate as the upper bound of the algorithm's retrieval ability. As described in Wentz and Spencer [13], because the retrieved rain rate is about 25 mm/h when \hat{A}_{L19} reaching the value of 1.2 for a rain column height of 3 km, the WS algorithm's retrieval ability is limited to 25 mm/h. For MWRI WS retrievals, the limit of retrieved rain rates is approximately 27 mm/h, as shown in Section 5.1.

Figure 3 shows the 37 GHz liquid water absorption versus 19 GHz absorption values, comparing with theoretical Mie absorption (black line), before (red line) and after (blue line) beamfilling correction. The curves are generated based on 101,879 MWRI observations. The \hat{A}_{L19} and \hat{A}_{L37} values curve closely follows the theoretical curve until the value of $A_{L19} \approx 0.4$. Above this value, the maximum value restriction of \hat{A}_{L37} becomes important and the curve value asymptotically approaches 1.2. The value of \hat{A}_{L37} is a constant (1.2) for the high absorption value.

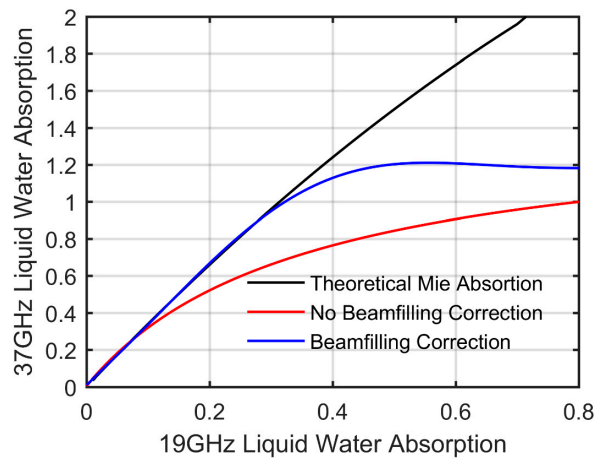


Figure 3. The 37 and 19 GHz liquid water absorption before (red line) and after (blue line) beamfilling correction compared with the theoretical Mie absorption (black line).

Finally, based on the assumption that surface rain rates equal vertically averaged rain rates, the basic Equations (10) and (11) are used to infer rain rate from liquid water attenuation (\hat{A}_{L19} and \hat{A}_{L37} , after beamfilling correction), which are described in [7]:

$$\hat{A}_{L19} = 0.0556[1 - 0.0288(T_L - 283)]L + 0.0113[1 + 0.004(T_L - 283)]HR^{1.0636}, \quad (10)$$

$$\hat{A}_{L37} = 0.2027[1 - 0.0261(T_L - 283)]L + 0.0425[1 - 0.002(T_L - 283)]HR^{0.9546}, \quad (11)$$

where L is columnar cloud water and H is the height of the rain column, which are factored out by [13]. Assuming the rain cloud temperature is the mean temperature of the surface and freezing level: $T_L = (T_S + 273)/2$.

5. Results

Because there are no in-situ observations to validate the retrievals for any TC case over oceans, we provide an intercomparison of the MWRI retrievals with other available remotely sensed datasets (see Section 3). Our evaluation consists of four separate parts. The first activity is to compare the MWRI rainfall retrieval to the NSIDC rain rate to see how they agree instantaneously using matched points from six selected TCs and find reasons for disagreements. The second is to examine the sensitivity of this algorithm by comparing AMSR-E Tbs rain retrievals with MWRI retrievals and see how well they match. The third part is to compare MWRI rain retrievals against TRMM PR rain rates. The final part focuses on the capability of MWRI retrievals in presenting the mesoscale structure of selected TCs compared with RSS TMI rainfall data.

5.1. Comparison with the NSIDC rainfall product

This comparison is established with 101,879 matched points of MWRI measurements and NSIDC rain rates from the six TCs. Figure 4 compares MWRI retrieved rain rates to the NSIDC rainfall data provided by the AMSR-E GPROF2010 algorithm.

Generally, MWRI rain retrievals are consistent with NSIDC rain rates in that they reproduce the main vortex structures of these selected TCs. In TCs, the rainfall outside the eyewall is primarily associated with a series of rainbands, which have a spiral geometry rather than the quasi-circular geometry of the eyewall [50]. Figure 4a,b show that the inner-core rainbands of TC Songda between MWRI and NSIDC data are consistent in rainfall distribution. However, the distant environmental regions near Taiwan island of these two figures show some differences. The eyes of TC Maon (Figure 4c,d) and TC Mufia (Figure 4e,f) are free of precipitation and are surrounded by eyewalls that contain intense rain rates and high wind speeds. The distant rainband near the inner-core region of TC Maon in Figure 4c shows consistency with that of the NSIDC product. The inner-core rainband around the eye of TC Mufia is consistent with the rainfall structure provided by NSIDC. TC Talas (Figure 4g,h) and TC Nesat (Figure 4k,l) have larger inner-core rainbands than other selected TCs, and the MWRI rainfall distributions of these two TCs show a good match with that of NSIDC in both inner-core and distant environmental regions. In TC Sonca (Figure 4i,j), there is no obvious eye in the TC vortex structure, and these two figures show the same distant rainbands in the northeastern quadrant and consistency in inner-core rainbands in the south quadrant. The MWRI retrievals show reasonable consistency with the NSIDC rainfall data in both inner-core and distant environment rainband distributions. The further statistical analysis of the MWRI retrieval is shown in Figures 5–7 and Table 3.

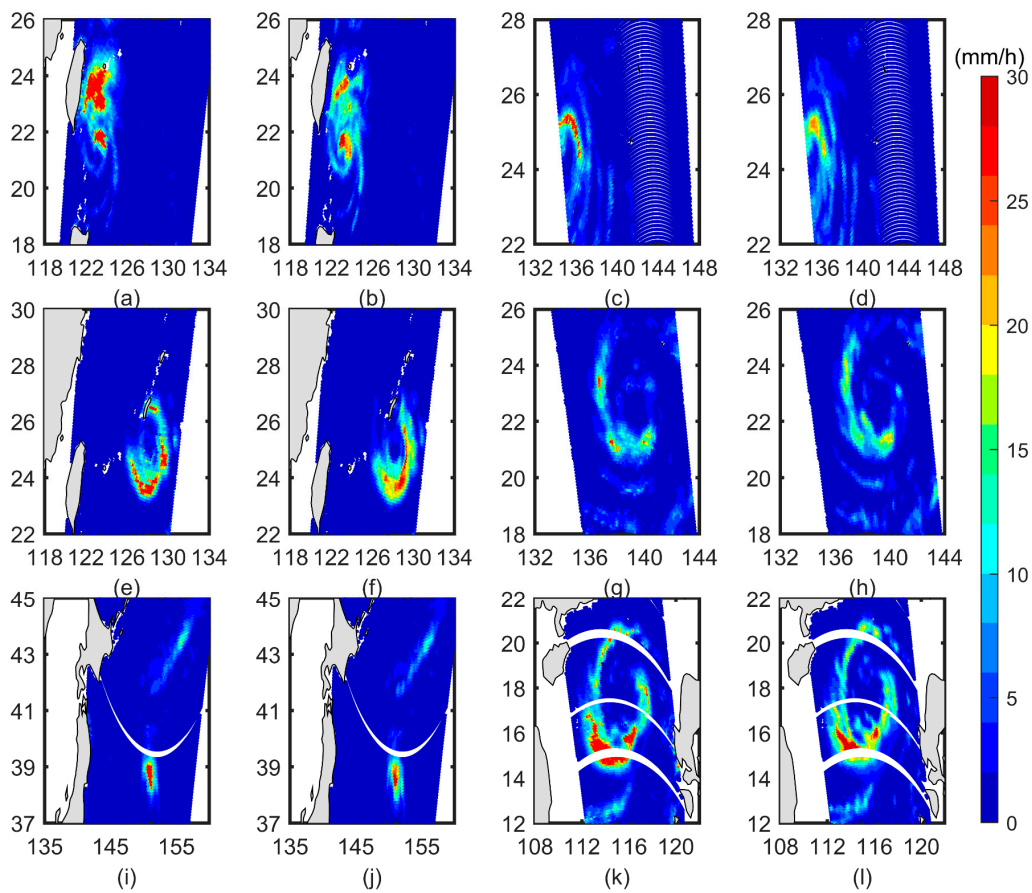


Figure 4. MWRI WS retrieved rain rate of six TCs versus the rain products provided by National Snow and Ice Data Center (NSIDC) data: (a) MWRI and (b) NSIDC Songda; (c) MWRI and (d) NSIDC Maon; (e) MWRI and (f) NSIDC Mufia; (g) MWRI and (h) NSIDC Talas; (i) MWRI and (j) NSIDC Sonca; (k) MWRI and (l) NSIDC Nesat. The blank spots in (a,b,e,f) are due to the missing sea surface temperature (SST), wind speed, water vapor data, land pixels, or no MWRI observations. The blank stripes in (i–l) are due to no MWRI observations.

Figure 5 shows pixel-to-pixel comparisons between MWRI rain retrievals and NSIDC rain rates for each TC. Two basic statistical measures—namely, the total bias and RMSE—are used to assess the performance of retrievals for each case. The negative total biases (title in Figure 5) are found in TCs, including Maon, Mufia, Talas, and Nesat, and they show that MWRI retrievals slightly underestimate rain intensities compared with the NSIDC product. Even if all the NSIDC rain rates (AMSR-E GPROF2010 product) within the MWRI 37 GHz FOV have been averaged before these comparisons, they still have higher rainfall resolution and therefore higher rain rates compared with MWRI retrievals. Figure 5 shows an obvious limited maximum rain rate (approximately 27 mm/h) at high intensities and shows underestimates at high rain rates for each case. As mentioned in Section 4, the limiting value for the maximum retrieved rain rate is mainly due to the saturation of frequencies. The retrievals of TC Songda (Figure 5a) and Sonca (Figure 5e) give positive total biases for 0.10 mm/h and 0.09 mm/h, respectively, which show a slight overestimation compared with NSIDC rain rates. Generally, the MWRI-retrieved rain rates show good agreement with the NSIDC product.

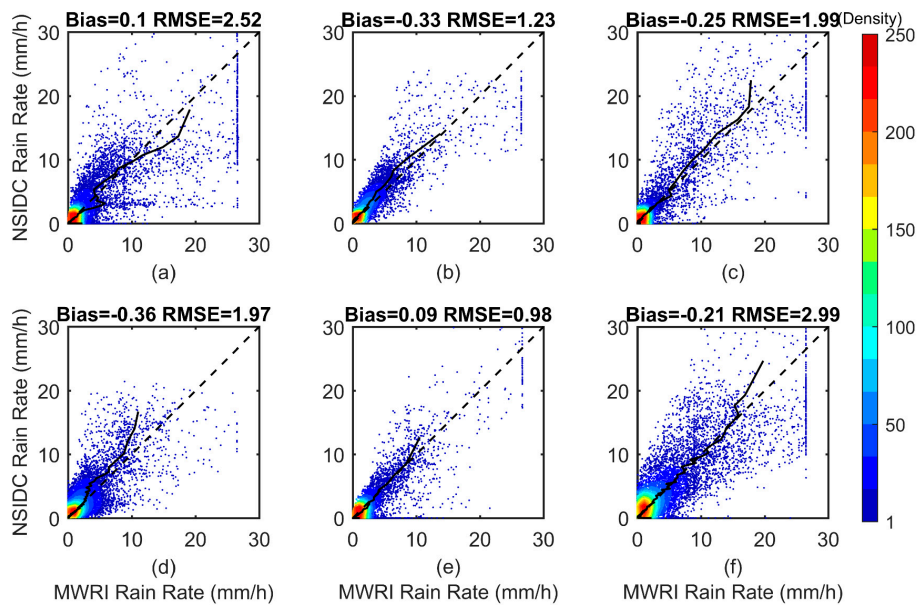


Figure 5. The pixel-to-pixel comparisons between the MWRI-retrieved rain rate and NSIDC rainfall product for each selected TC: (a) Songda; (b) Maon; (c) Mufia; (d) Talas; (e) Sonca; (f) Nesat. The mean of MWRI retrievals (solid line) and 1:1 line (dashed line) are presented in each plot.

The occurrences of MWRI surface rain rates versus NSIDC rain rates are presented in Figure 6. The histograms of these six TCs do not differ much in the low rain rate distribution of each TC but change significantly at the high rain intensity distribution. In particular, the number of the maximum MWRI-retrieved rain rates (approximately 27 mm/h) in Songda (Figure 6a), Mufia (Figure 6c), and Nesat (Figure 6f) are both over 100 compared with other cases. It can be seen that the performance of MWRI retrievals is relatively consistent with the rainfall products in histograms.

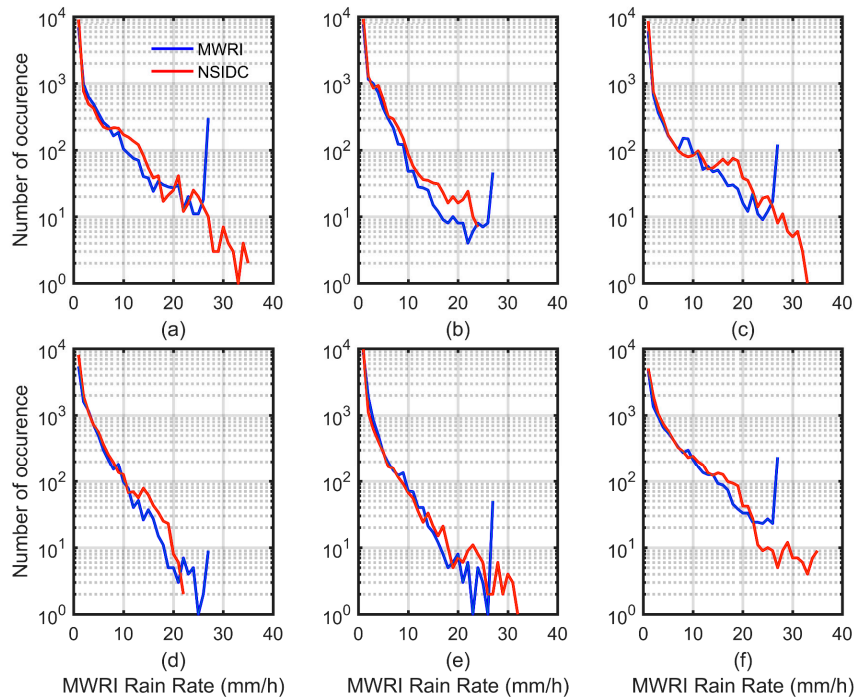


Figure 6. Histograms of FY-3B MWRI retrievals versus precipitation products provided by NSIDC for six selected TCs: (a) Songda; (b) Maon; (c) Mufia; (d) Talas; (e) Sonca; (f) Nesat.

To assess the total rain intensity distribution between the MWRI retrieved rain rate and the NSIDC rain rate for all cases, the total pixel-to-pixel scatter plot and statistic evaluation are displayed in Figure 7 and Table 3. Figure 7 exhibits relatively consistent performance between the MWRI retrievals and NSIDC rainfall product. The scatter in this figure can be attributed to the differences in the sampling of these two instruments and differences between the retrieval algorithms. The mean rain rates of MWRI retrievals (dashed line) compared with the one-to-one line are depicted, and this shows that the MWRI WS algorithm tends to underestimate the rain rates of 5–0 mm/h and over 15 mm/h.

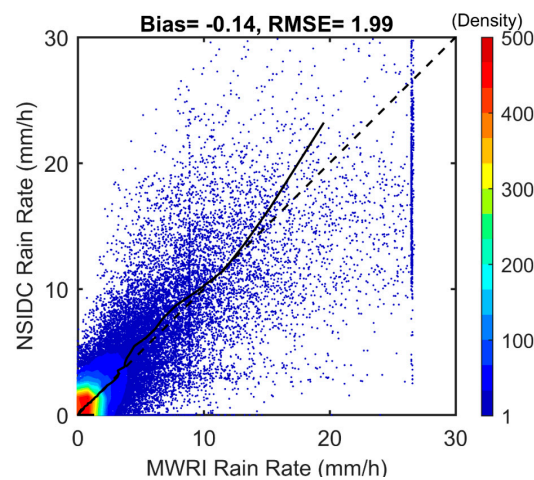


Figure 7. The pixel-to-pixel comparisons between the MWRI-retrieved rain rate and NSIDC rainfall product for all six TCs. The mean of MWRI retrieval line (solid line) and 1:1 line (dashed line) are shown.

To analyze the statistical quality of MWRI retrievals, the bias, RMSE, and bias percentage values between the MWRI rain rates and NSIDC rain rates for all TCs are shown in Table 3. The overall mean bias and RMSE of the MWRI retrievals for all six TCs are -0.14 mm/h and 1.99 mm/h, respectively, which shows an encouraging accuracy compared to the NSIDC rain intensity. Biases of different rainfall categories between these two rain products are almost negative, except the 1.0 – 0 mm/h and 2.0 – 3.0 mm/h rainfall categories, which is due to a few factors. The NSIDC rain rate estimates a higher rain rate than that of MWRI because the AMSR-E GPROF2010 algorithm has a smaller FOV (5 km \times 10 km) compared with that of MWRI WS algorithm (18 km \times 30 km). In the GPROF2010 scheme, different combinations of all AMSR-E channel frequencies are used, while there are only two low frequencies applied to the MWRI WS algorithm. Consequently, the fundamental observation–rainfall relationship will be different.

The MWRI retrievals show reasonable levels for most rain categories because the absolute value of bias percentage in each category is lower than 15% except for the 0.0 – 0.5 mm/h and 25 – 30 mm/h categories. The 0.0 – 0.5 mm/h category has a bias percentage of -21.4% . The 10 – 15 mm/h category holds a bias percentage of -1.1% and performs well regarding the retrieved results with NSIDC rain rates. The mean rain rate of MWRI retrievals is about 8.7% lower than that of NSIDC rain rates at the 15 – 25 mm/h category, which shows a good match with NSIDC rain rates. The bias percentage of the 25 – 30 mm/h category is -22.8% which shows an underestimation of MWRI retrieval over the WS algorithm’s limited rain rate. Saturation in the MWRI WS algorithm limits the maximum rain intensity.

Table 3. Quantitative assessment of MWRI retrievals compared with NSIDC rain rates for the six selected TCs combined. The rain interval, the number of pixels, mean rain rates, bias (MWRI–NSIDC), bias percentage $((\text{MWRI} - \text{NSIDC}) / \text{NSIDC} \times 100\%)$, and total RMSE are listed. The unit is mm/h except for bias percentage.

Rain Interval	Pixel Number	MWRI Retrievals	NSIDC Rain Rate	Bias	Bias Percentage
0.0–0.5	55,172	0.11	0.14	−0.03	−21.4%
0.5–1.0	10,794	0.65	0.71	−0.06	−8.4%
1.0–2.0	7711	1.46	1.43	0.03	2.1%
2.0–3.0	4555	2.57	2.48	0.09	3.6%
3.0–4.0	3500	3.35	3.47	−0.12	−3.4%
4.0–6.0	4076	4.18	4.87	−0.69	−14.1%
6.0–8.0	2445	6.17	6.94	−0.77	−11.1%
8.0–10.0	1671	8.34	8.95	−0.71	−7.9%
10.0–15.0	2356	12.07	12.21	−0.14	−1.1%
15.0–25.0	1629	16.80	18.40	−1.60	−8.7%
25.0–30.0	237	21.00	27.20	−6.20	−22.8%
Total bias: −0.14			Total RMSE: 1.99		

5.2. Comparison with AMSR-E Tbs Retrievals

Because the MWRI and AMSR-E instruments have the same LTAN and viewing geometries, the collocations of these two instruments are close. To assess the application of the MWRI WS algorithm to other sensors, the AMSR-E Tbs provided by the NSIDC are used as input data for this algorithm to get rainfall retrievals utilizing the matched points between MWRI, AMSR-E observations, and NSIDC rain rates for the six TCs. Since the retrieved results are derived from the same algorithm and parameters, the comparison between MWRI and AMSR-E retrievals is not a rigorous test, but rather a consistency check.

Table 4 shows the rain retrievals of MWRI and AMSR-E measurements compared with the NSIDC rain rates, respectively. The overall mean RMSE of rain rates between MWRI retrievals and NSIDC rain rates is much lower than that of AMSR-E observations (1.99 mm/h and 3.11 mm/h, respectively). The bias of AMSR-E retrievals is 0.90 mm/h, which is much higher than that of MWRI. Each individual case has a similar result regarding the total bias and RMSE. The RMSE of TC Nesat in MWRI retrievals is 2.99 mm/h, which is the highest RMSE in MWRI-retrieved results and much lower than that of AMSR-E (4.49 mm/h). The minimum RMSE of the MWRI-retrieved rain rates of 0.98 mm/h occurred in TC Sonca, which is nearly half of AMSR-E (2.00 mm/h). In addition, all the biases of AMSR-E retrievals are positive, which shows an overestimation of rain retrievals.

Table 4. Statistical errors of MWRI and AMSR-E retrievals against the NSIDC product (mm/h).

TC's Name	MWRI		AMSR-E	
	Bias	RMSE	Bias	RMSE
Songda	0.01	2.52	1.11	3.63
Maon	−0.33	1.23	0.51	2.48
Mufia	−0.25	1.99	0.73	3.22
Talas	−0.36	1.97	0.85	2.84
Sonca	0.09	0.98	0.65	2.00
Nesat	−0.21	2.99	1.74	4.49
Total	−0.14	1.99	0.90	3.11

The overestimation of the AMSR-E-retrieved rain rates for the six TCs is mainly attributed to two factors. The first reason is due to the vertical Tbs (Figure 8a) of AMSR-E from the six TCs being about 5 K higher than that of MWRI, while the horizontal Tbs (Figure 8b) of both instruments are nearly the same. Secondly, the MWRI algorithm implemented in this paper does not explicitly account for the

resolution of AMSR-E footprint. The beamfilling correction works well for MWRI resolution (Table 1), but it assumes more spatial variability when it is actually present in a smaller footprint of AMSR-E. Therefore, the beamfilling correction tends to overcorrect AMSR-E rainfall retrievals, similar to the behavior shown in [25]. Because it neglects the resolution dependence in the beamfilling correction during the rain retrieval algorithm, the AMSR-E instrument with higher retrieval resolution has higher biases than that of MWRI.

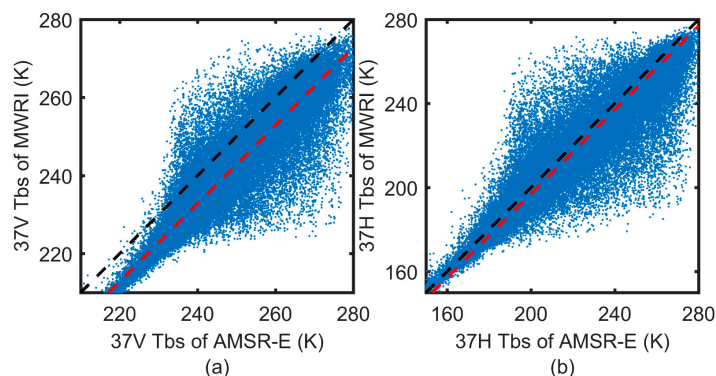


Figure 8. The Tb biases of AMSR-E and MWRI sensors (red dashed line), and 1:1 line (black dashed line) are depicted: (a) vertical; (b) horizontal.

5.3. Case Study: Comparison with TRMM PR data for Maon

So far, we have assessed the MWRI rain rates against other passive microwave retrievals. In this section, we compare MWRI rain rates against active microwave retrievals. Using the matchup method described in Section 3, we only get one TC (TC Maon) to make a comparison between MWRI retrieved rain rates and TRMM PR observations due to the narrow swath of PR. The MWRI and PR observation time difference of TC Maon is approximately 19 min.

Figures 9 and 10 present the comparison of the MWRI-retrieved rain rates and NSIDC rainfall product with PR precipitation for TC Maon, respectively, and show the differences between these products organized with storm scales. MWRI retrievals and NSIDC rainfall data are higher in the eyewall and PR rain rates are higher in distant rainbands. The performance of MWRI retrievals and NSIDC rain rates for TC Maon shows good agreement with PR rain intensities on the storm scale. Regional biases can occur because of the differences in these retrieval algorithms. The PR algorithm determines rain rates based on the relationship between reflectivity and rain rate [39], while the WS algorithm retrieves rain rates utilizing the relationship between liquid water absorption and rain rate [13], and the AMSR-E GPROF2010 algorithm is a Bayesian retrieval scheme mainly based on the priori oceanic database created for AMSR-E [28].

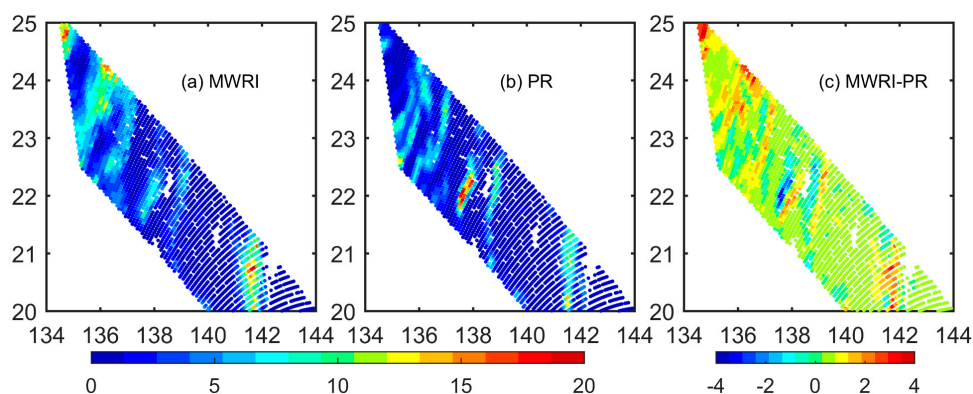


Figure 9. The rain rate (mm/h) comparison of TC Maon: (a) the MWRI retrieved rain rates; (b) TRMM Precipitation Radar (PR) rainfall product; (c) the MWRI-PR rainfall difference for Maon. The blank spots in figures are the missing MWRI retrieval pixels.

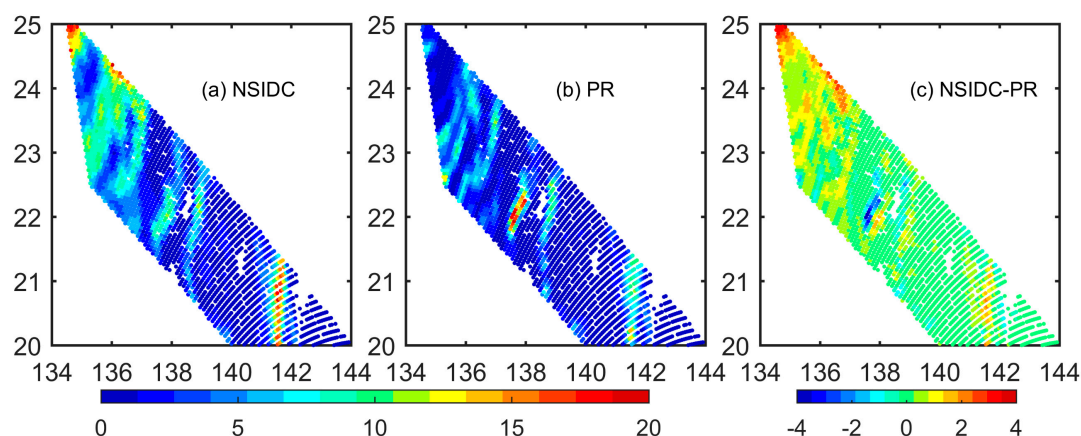


Figure 10. As in Figure 9, but for NSIDC rain rate (mm/h): (a) the NSIDC rain rates; (b) TRMM PR rainfall product; (c) the NSIDC–PR rainfall difference for Maon.

Table 5 shows the bias and RMSE values of MWRI retrievals and NSIDC rain rates with PR rain rates for different rain categories, respectively. For MWRI retrievals, the maximum error of -8.79 mm/h is reached at the rain category of 10–25 mm/h, and the biases for rain categories below (over) 6 mm/h are positive (negative). The NSIDC rain rates show an underestimation at rain rates over 8 mm/h and overestimation below 8 mm/h.

The overestimate of the MWRI-retrieved rain rates lower than 6 mm/h is likely due to overcorrecting the beamfilling effect for MWRI. Additionally, the PR algorithm described in detail by [39] uses an a priori drop size distribution for light and moderate rain rates (<5 mm/h), while it corrects the attenuation of the radar beam for the heavy rainfall [26]. Both factors can introduce errors to PR products and introduce biases when comparing with MWRI and NSIDC rain intensities. The underestimation of MWRI and NSIDC rain rates is mainly ascribed to the larger footprint than that of PR ($5 \text{ km} \times 5 \text{ km}$). This can be expected as a radiometer is not as capable a rain sensor as the PR, even if is averaged to the same spatial resolution. While PR shows low sensitivity to low rain rates, it is sensitive to high rain intensities and gives good measurements of heavy rainfall. The MWRI WS algorithm determines heavy rain intensities using the relationship between the liquid water absorption (FOV averaged to MWRI 37 GHz) and rain rates, which leads to a lower rate of heavy rain rate than that of PR. For NSIDC, the underestimation of high rain intensity is mainly due to the fewer rainfall profiles in the oceanic database, which determines the retrieval accuracy of the GPROF2010 algorithm [28].

Table 5. The pixel number, PR average rain rate, averaged rain rate MWRI and NSIDC, and bias (MWRI-PR and NSIDC-PR) of MWRI and NSIDC rain rates with PR rain rates, respectively, for each rain interval, and the total bias and RMSE of MWRI and NSIDC rain rates compared with PR, respectively. The unit is mm/h except for the pixel number.

Rain Interval	Pixel Number	PR Rain Rate	MWRI		NSIDC	
			Rain Rate	Bias	Rain Rate	Bias
0.0–0.5	797	0.18	0.73	0.55	0.99	0.81
0.5–1.0	338	0.74	1.91	1.17	2.34	1.60
1.0–2.0	420	1.47	2.89	1.42	3.69	2.22
2.0–3.0	248	2.50	3.76	1.26	4.56	2.06
3.0–4.0	201	3.47	4.90	1.43	5.78	2.31
4.0–6.0	295	4.89	5.25	0.34	6.26	1.37
6.0–8.0	53	7.42	6.27	-1.15	8.43	1.01
8.0–10.0	17	9.48	5.73	-3.75	9.20	-0.28
10.0–25.0	27	13.76	4.97	-8.79	7.34	-6.42
			Total bias:	0.74		1.41
			Total RMSE:	2.40		2.64

5.4. Mesoscale Structure of the Selected TCs

To check whether the saturation of the MWRI WS algorithm could impact the structure of TCs, the RSS TMI rainfall product is selected and used as evaluation data. To assess the capability of MWRI retrievals in presenting the mesoscale structure of intense TCs, the resulting rain fields of the MWRI-retrieved rain rates and the TMI rainfall data are shown in Figures 11 and 12, respectively. They not only offer a series of well-defined characteristic structures, but also a large range of rain intensities. These two figures are differently color-coded because the TMI rainfall data are gridded data, which have lower rain rates than MWRI retrievals. This section is not intended to compare the rainfall deviation between MWRI retrievals and TMI gridded rainfall data, but to check whether the TC structures of MWRI retrievals match TMI rain rates.

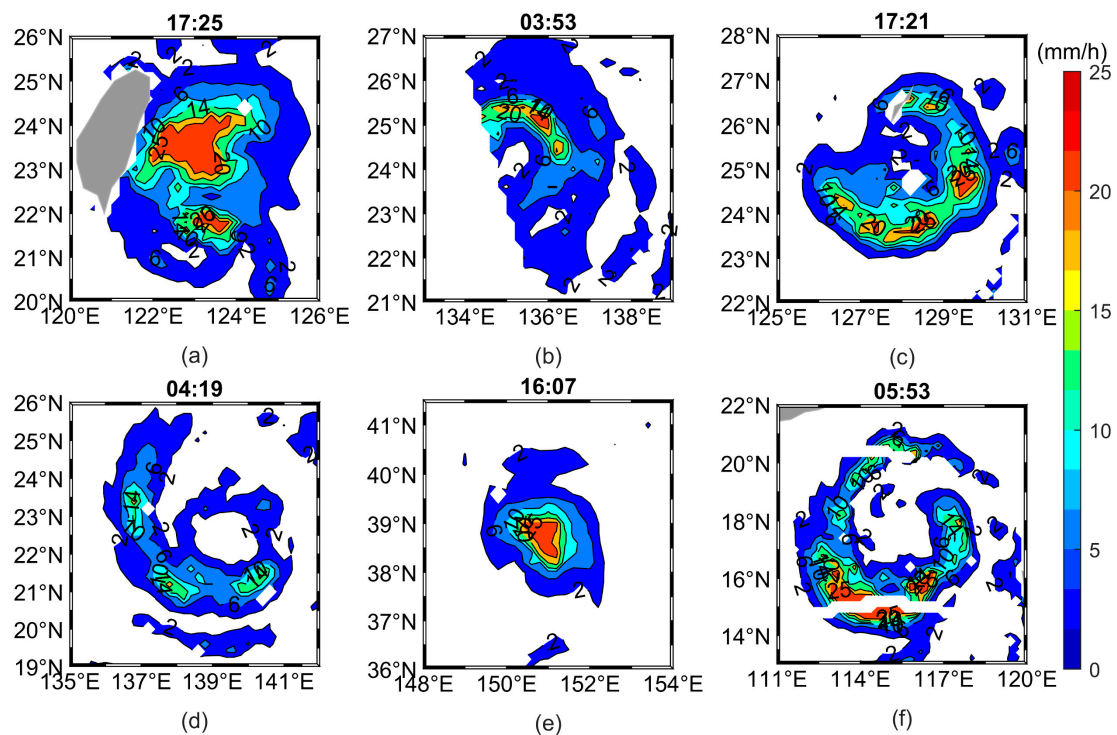


Figure 11. MWRI retrieval counters for six selected track records: (a) Sonda; (b) Maon; (c) Mufia; (d) Talas; (e) Sonca; (f) Nesat. The blank stripes in (f) are due to the missing MWRI observations. The title in each TC is the start scan time of MWRI observation in the plotted area.

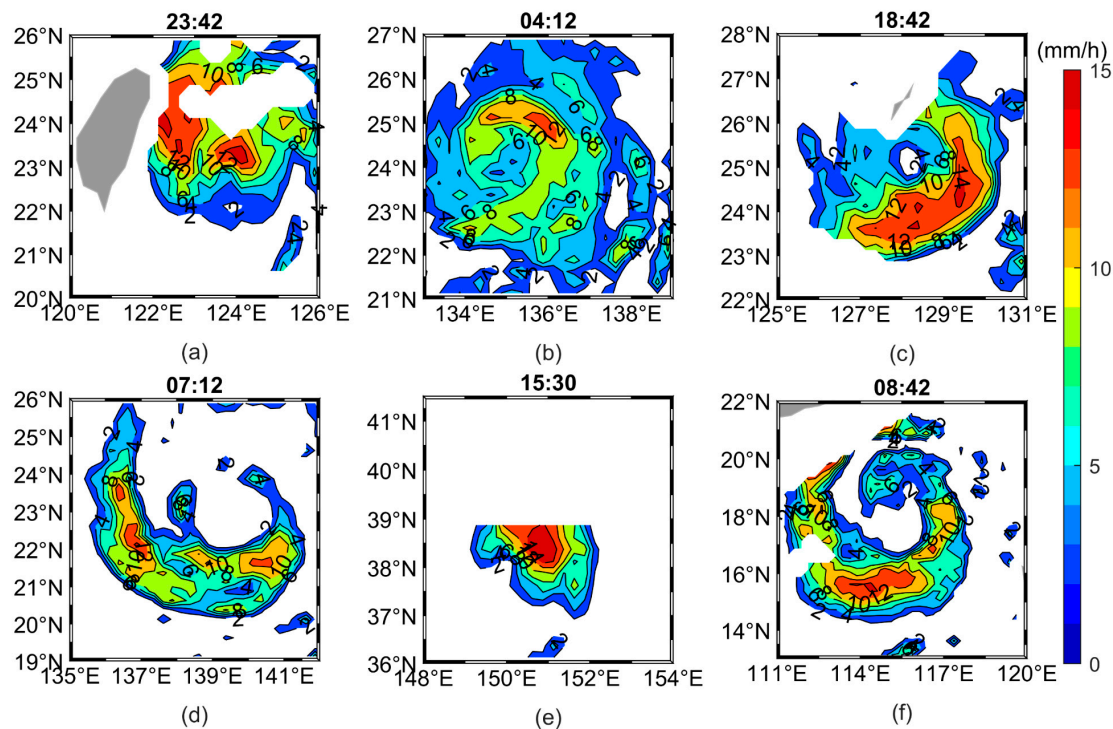


Figure 12. Remote Sensing Systems (RSS) TMI rainfall counters: (a) Sonda; (b) Maon; (c) Mufia; (d) Talas; (e) Sonca; (f) Nesat. The blank spots in (a), (c), (e), and (f) are due to the missing SST, wind speed, water vapor data, land pixels, or no TMI observations. The title in each TC is the start scan time of TMI gridded data in the plotted area.

The performance of these two precipitation products shows that MWRI retrievals represent clear mesoscale structures of the selected TCs. Figure 11a shows the retrieved rainfall structure of Songda from MWRI: a principal rainband near eyewall with 20 mm/h contour surrounds, and a broader distant rainband near Taiwan island. Even though the time difference of MWRI and TMI observations is approximately 6 h, TMI (Figure 12a) shows a similar rainband structure, which is partially obscured by more aggressive land masking of the Yaeyama and Miyako Islands. TC Maon (Figure 11b) indicates a clearly visible TC eye, which is free of precipitation and surrounded by an intense eyewall. The 20 mm/h rainfall contour of Maon corresponds to an eyewall region, and similarly, the maximum contour (12 mm/h) of TMI rain intensities (Figure 12b) occurs in the north-eastern quadrant. TMI shows a broader area of moderate rain rates in the distant rainband (the south-eastern quadrant). These two figures (Figures 11b and 12b) have the minimum time difference (~19 min), and TC Maon does not move a large distance. The structures of Mufia from MWRI and TMI (Figures 11c and 12c) are in relatively good agreement within a 1.5-h time difference. The inner-core structure of Mufia from MWRI (Figure 11c) is clear, with a 10 mm/h rainfall contour corresponding to the vortex region and high rain rates of 10 to 20 mm/h that extend to the most of Mufia structure, particularly in the southeast quadrant.

The rain field structure of Talas from MWRI (Figure 11d) has a larger TC scale; however, its retrieved rain rates are lower than other cases. TMI (Figure 12d) exhibits three relative maxima in the western, south-western, and south-eastern parts of the storm, in agreement with MWRI. The TC Sonca from MWRI (Figure 11e) within a 30-min time difference is the smallest storm among all the cases, and its rainfall distribution is extremely compact with low rain rates between 0 and 10 mm/h extending over the inner-core structure of the TC system, and TMI has the same compact structure (Figure 12e). The structure of TC Nesat from MWRI (Figure 11f) displays the main vortex zone with 25 mm/h contour corresponding to the TC eyewall. Despite the missing MWRI scans, the mainly high rainband shows a broad principal rainband of Nesat. TMI has a similar area of high rain rates along the southern

portion of the storm (Figure 12f). The results show that the saturation of MWRI WS algorithm does not impact the structure of TCs, and MWRI retrievals present clear mesoscale structures of intense TCs.

6. Discussion

Our results have shown that a rain retrieval algorithm closely based on the WS algorithm, applied to MWRI measurements, provides reasonable rain rates for TCs and well represents the TC mesoscale structures. The WS algorithm is a physical scheme based on dual-polarization passive microwave measurements to provide a two-way transmittance through the atmosphere. The advantage of this simple strategy is that the parameterizations are more tightly constrained [25]. However, this retrieval algorithm applied to MWRI still shows some problems. The MWRI retrievals were low relative to the NSIDC dataset in high intensities. However, positive mean differences were found when the same algorithm was applied to AMSR-E measurements. The retrievals did not match from different sensors because the WS algorithm did not include the resolutions of different sensors in the beamfilling correction. The unified microwave ocean retrieval algorithm (UMORA) algorithm developed by Hilburn and Wentz [25] is an improvement of the WS algorithm in that it corrects this problem. For practical applications of the new rain retrieval algorithm, it is planned to apply the UMORA algorithm to MWRI measurements for TCs.

Although the MWRI retrievals for six selected TCs shown in Figure 7 provides consistent performance with the NSIDC rainfall product from the GPROF2010 algorithm, there are some differences due to fundamental algorithm differences. GPROF retrieves a higher surface rain rate compared with MWRI because of differences in microphysical assumptions. In the GPROF algorithm, the vertical rain water profile is more physically constrained, while the WS algorithm assumes a constant vertical precipitation profile and thus obtains a surface rain rate that is equal to the column-average rain rate. Another issue is that it does not explicitly account for the spatial resolution of the satellite observations. Hilburn and Wentz [25] found that the probability distribution function $P(A')$ (see Equation (5)) changes systematically with the footprint size. The WS algorithm assumed that this distribution function works well for SSM/I resolution (37 GHz, 28 km × 37 km); however, it assumes more spatial variability than in the smaller AMSR-E footprint (37 GHz, 8 km × 14 km). Thus, the beamfilling overcorrected AMSR-E. As shown in Table 4, the rain retrievals from the higher-resolution sensor (AMSR-E) are biased higher than MWRI retrievals if the resolution dependence in the beamfilling correction is neglected. While the MWRI instrument has a similar resolution (37 GHz, 18 km × 30 km) to SSM/I, it works better in the WS algorithm than the AMSR-E instrument.

7. Conclusions

With the development of passive microwave radiometers, retrieving rain rates inside TCs has become possible. The goal of this study is to develop an algorithm for estimating surface rain rates of TCs using 19 and 37 GHz V and H polarized Tbs from FY-3B MWRI. Based on the algorithm derived by Wentz and Spencer [13], an ocean-only rainfall retrieval algorithm for the MWRI has been developed. Since the nonlinear relationship between rain rate and Tb occurs when averaging over the radiometer footprint, the beamfilling correction is considered by comparing ratios of liquid water absorption with the theoretical Mie absorption between 37 and 19 GHz.

MWRI WS retrievals are in reasonable agreement with other datasets. The MWRI measurements for six selected TCs and rain rates provided by the NSIDC are used to develop and verify the accuracy of this retrieval algorithm. The results are encouraging, with an overall mean bias and RMSE of −0.14 mm/h and 1.99 mm/h, respectively. The histograms of these two products for six TCs show encouraging agreement and do not differ much at the low rain rate distribution of each TC; however, they differ more at high rain intensity distribution. A comparison of instantaneous pixel-to-pixel retrievals shows that the MWRI retrieval shows reasonable agreement for most rain categories with absolute bias percentages within 15%, except for the lowest (0–0.5 mm/h) and highest (25–30 mm/h)

rain rates (−21.4% and −22.8%, respectively). The maximum rain rate value (~27 mm/h) of MWRI retrievals is limited due to the frequency saturation.

To assess the sensitivity of the MWRI WS algorithm to the sensor configuration, the algorithm was also applied to AMSR-E Tbs. The overall mean bias and RMSE are 0.90 mm/h and 3.11 mm/h, respectively, which are higher than that of MWRI retrievals. The AMSR-E WS retrievals overestimate rain rates compared with the NSIDC rain rate. A case study for TC Maon (2011) showed that MWRI WS retrievals agree well with PR rain rates on storm scales; however, MWRI rain rates overestimate rain rates below 6 mm/h and underestimate over 6 mm/h relative to PR rain rates. Additionally, the RSS TMI rainfall product is used to assess the capability of the MWRI WS algorithm in representing the mesoscale structure of rain rates in intense TCs. The performance of MWRI retrievals shows the clear mesoscale structures of the selected TCs. Despite the remaining uncertainties in the MWRI WS rainfall retrieval, the reasonable intercomparison of datasets indicates that the retrieved rain rate can be used for the TCs' surface precipitation and mesoscale structure studies. The MWRI sensor performs well and provides good quality Tbs.

Author Contributions: Data curation, R.Z.; formal analysis, R.Z. and K.A.H.; funding acquisition, Z.W.; investigation, R.Z.; methodology, R.Z. and K.A.H.; project administration and resources, Z.W.; software, R.Z. and K.A.H.; supervision, Z.W.; validation and visualization, R.Z.; writing—original draft preparation, R.Z.; writing—review & editing, R.Z., Z.W., and K.A.H.

Funding: This research was funded by the National Natural Science Foundation of China grant number 61501433.

Acknowledgments: The authors would like to thank the National Satellite Meteorological Center Feng Yun Satellite Data Center, the National Centers for Environmental Prediction, the National Snow and Ice Data Center, the NASA Precipitation Measurement Missions team, and the Remote Sensing Systems for providing the satellite datasets and the JTWC team for the provision of best-track data for TCs.

Conflicts of Interest: The authors declare no conflict of interest. The funding sponsors had no role in the design of the study; in the collection, analyses, or interpretation of data; in the writing of the manuscript, and in the decision to publish the results.

References

1. Gray, W.M. Global view of origin of tropical disturbances and storms. *Mon. Weather Rev.* **1968**, *96*, 669–700. [[CrossRef](#)]
2. Cutter, S.L.; Emrich, C.T. Moral hazard, social catastrophe: The changing face of vulnerability along the hurricane coasts. *Ann. Am. Acad. Political Soc. Sci.* **2006**, *604*, 102–112. [[CrossRef](#)]
3. Zick, S.E.; Matyas, C.J. A shape metric methodology for studying the evolving geometries of synoptic-scale precipitation patterns in tropical cyclones. *Ann. Am. Assoc. Geogr.* **2016**, *106*, 1217–1235. [[CrossRef](#)]
4. Shige, S.; Takayabu, Y.N.; Tao, W.-K.; Johnson, D.E. Spectral retrieval of latent heating profiles from TRMM PR data. Part I: Development of a model-based algorithm. *J. Appl. Meteorol.* **2004**, *43*, 1095–1113. [[CrossRef](#)]
5. Atlas, D.; Thiele, O.W. Precipitation Measurements from Space. In Proceedings of the IEEE International Geoscience and Remote Sensing Symposium, NASA/Goddard Space Flight Center, Greenbelt MD, USA, 1 October 1981; p. 441.
6. Milman, A.S.; Wilheit, T.T. Sea surface temperatures from the scanning multichannel microwave radiometer on Nimbus 7. *J. Geophys. Res.* **1985**, *90*, 11631. [[CrossRef](#)]
7. Wentz, F.J.; Meissner, T. *AMSR Ocean Algorithm Theoretical Basis Document, Version 2*; Remote Sensing Systems: Santa Rosa, CA, USA, November 2000.
8. Kidd, C.; Matsui, T.; Chern, J.; Mohr, K.; Kummerow, C.D.; Randel, D.L. Global precipitation estimates from cross-track passive microwave observations using a physically based retrieval scheme. *J. Hydrometeorol.* **2016**, *17*, 383–400. [[CrossRef](#)]
9. Petković, V.; Kummerow, C.D.; Randel, D.L.; Pierce, J.R.; Kodros, J.K. Improving the quality of heavy precipitation estimates from satellite passive microwave rainfall retrievals. *J. Hydrometeorol.* **2018**, *19*, 69–85. [[CrossRef](#)]
10. Kidd, C.; Levizzani, V. Status of satellite precipitation retrievals. *Hydrol. Earth Syst. Sci.* **2011**, *15*, 1109–1116. [[CrossRef](#)]

11. Basharinov, A.; Yegorov, S.; Gurvich, A.; Oboukhov, A. Some results of microwave sounding of the atmosphere and ocean from the satellite Cosmos 243. *Space Res.* **1971**, *11*, 593–600.
12. Hollinger, J.P.; Peirce, J.L.; Poe, G.A. SSM/I instrument evaluation. *IEEE Trans. Geosci. Remote Sens.* **1990**, *28*, 781–790. [[CrossRef](#)]
13. Wentz, F.J.; Spencer, R.W. SSM/I rain retrievals within a unified all-weather ocean algorithm. *J. Atmos. Sci.* **1998**, *55*, 1613–1627. [[CrossRef](#)]
14. Kummerow, C.D.; Barnes, W.; Kozu, T.; Shiue, J.; Simpson, J. The Tropical Rainfall Measuring Mission (TRMM) sensor package. *J. Atmos. Ocean. Technol.* **1998**, *15*, 809–817. [[CrossRef](#)]
15. Hou, A.Y.; Kakar, R.K.; Neeck, S.; Azarbarzin, A.A.; Kummerow, C.D.; Kojima, M.; Oki, R.; Nakamura, K.; Iguchi, T. The Global Precipitation Measurement Mission. *Bull. Am. Meteorol. Soc.* **2014**, *95*, 701–722. [[CrossRef](#)]
16. Huffman, G.J.; Bolvin, D.T.; Braithwaite, D.; Hsu, K.; Joyce, R.; Kidd, C.; Nelkin, E.J.; Xie, P. *NASA Global Precipitation Measurement Integrated Multi-Satellite Retrievals for GPM (IMERG) Algorithm Theoretical Basis Document (ATBD) Version 4.5*; National Aeronautics and Space Administration: Washington, DC, USA, November 2015.
17. Kawanishi, T.; Sezai, T.; Ito, Y.; Imaoka, K.; Takeshima, T.; Ishido, Y.; Shibata, A.; Miura, M.; Inahata, H.; Spencer, R.W. The Advanced Microwave Scanning Radiometer for the Earth Observing System (AMSR-E), NASDA's contribution to the EOS for global energy and water cycle studies. *IEEE Trans. Geosci. Remote Sens.* **2003**, *41*, 184–194. [[CrossRef](#)]
18. Yang, H.; Weng, F.; Lv, L.; Lu, N.; Liu, G.; Bai, M.; Qian, Q.; He, J.; Xu, H. The FengYun-3 Microwave Radiation Imager on-orbit verification. *IEEE Trans. Geosci. Remote Sens.* **2011**, *49*, 4552–4560. [[CrossRef](#)]
19. Buettner, K.J.K. Regenortung vom wettersatelliten mit hilfe von zentimeterwellen (Rain localization from a weather satellite via centimeter waves). *Naturwiss* **1963**, *50*, 591–592. [[CrossRef](#)]
20. Grody, N.C. Classification of snow cover and precipitation using the Special Sensor Microwave Imager. *J. Geophys. Res. Atmos.* **1991**, *96*, 7423–7435. [[CrossRef](#)]
21. Ferraro, R.R.; Marks, G.F. The development of SSM/I rain-rate retrieval algorithms using ground-based radar measurements. *J. Atmos. Ocean. Technol.* **1995**, *12*, 755–770. [[CrossRef](#)]
22. Spencer, R.W.; Goodman, H.M.; Hood, R.E. Precipitation retrieval over land and ocean with the SSM/I: Identification and characteristics of the scattering signal. *J. Atmos. Ocean. Technol.* **1989**, *6*, 254–273. [[CrossRef](#)]
23. Kidd, C. On rainfall retrieval using polarization-corrected temperatures. *Int. J. Remote Sens.* **1998**, *19*, 981–996. [[CrossRef](#)]
24. Brown, P.J.; Kummerow, C.D.; Randel, D.L. Hurricane GPROF: An optimized ocean microwave rainfall retrieval for tropical cyclones. *J. Atmos. Ocean. Technol.* **2016**, *33*, 1539–1556. [[CrossRef](#)]
25. Hilburn, K.A.; Wentz, F.J. Intercalibrated passive microwave rain products from the Unified Microwave Ocean Retrieval Algorithm (UMORA). *J. Appl. Meteorol. Climatol.* **2008**, *47*, 778–794. [[CrossRef](#)]
26. Kummerow, C.D.; Hong, Y.; Olson, W.S.; Yang, S.; Adler, R.F.; McCollum, J.; Ferraro, R.; Petty, G.; Shin, D.B.; Wilheit, T.T. The evolution of the Goddard profiling algorithm (GPROF) for rainfall estimation from passive microwave sensors. *J. Appl. Meteorol.* **2001**, *40*, 1801–1820. [[CrossRef](#)]
27. Kummerow, C.D.; Randel, D.L.; Kulie, M.; Wang, N.Y.; Ferraro, R.; Munchak, S.J.; Petkovic, V. The evolution of the Goddard Profiling Algorithm to a fully parametric scheme. *J. Atmos. Ocean. Technol.* **2015**, *32*, 2265–2280. [[CrossRef](#)]
28. Kummerow, C.D.; Ringerud, S.; Crook, J.; Randel, D.; Berg, W. An observationally generated a priori database for microwave rainfall retrievals. *J. Atmos. Ocean. Technol.* **2011**, *28*, 113–130. [[CrossRef](#)]
29. Wilheit, T.; Kummerow, C.D.; Ferraro, R. Rainfall algorithms for AMSR-E. *IEEE Trans. Geosci. Remote Sens.* **2003**, *41*, 204–214. [[CrossRef](#)]
30. Li, X.; Zhao, F. Characteristics of precipitating clouds in typhoon Ma-on from MWRI and TMI observations. In Proceedings of the Remote Sensing, Environment and Transportation Engineering (RSETE), Nanjing, China, 1–3 June 2012; pp. 1–4.
31. Zhang, R.; Wang, Z.; Zhang, L.; Li, Y. Rainfall retrieval of tropical cyclones using FY-3B microwave radiation imager (MWRI). In Proceedings of the Geoscience and Remote Sensing Symposium (IGARSS), Fort Worth, TX, USA, 23–28 July 2017; pp. 550–553.

32. Knapp, K.R.; Kruk, M.C.; Levinson, D.H.; Diamond, H.J.; Neumann, C.J. The international best track archive for climate stewardship (IBTrACS) unifying tropical cyclone data. *Bull. Am. Meteorol. Soc.* **2010**, *91*, 363–376. [[CrossRef](#)]
33. Liu, C.; Zipser, E.J.; Cecil, D.J.; Nesbitt, S.W.; Sherwood, S. A cloud and precipitation feature database from nine years of TRMM observations. *J. Appl. Meteorol. Climatol.* **2008**, *47*, 2712–2728. [[CrossRef](#)]
34. Viltard, N.; Burlaud, C.; Kummerow, C.D. Rain retrieval from TMI brightness temperature measurements using a TRMM PR-based database. *J. Appl. Meteorol. Climatol.* **2006**, *45*, 455–466. [[CrossRef](#)]
35. Kummerow, C.D.; Olson, W.S.; Giglio, L. A simplified scheme for obtaining precipitation and vertical hydrometeor profiles from passive microwave sensors. *IEEE Trans. Geosci. Remote Sens.* **1996**, *34*, 1213–1232. [[CrossRef](#)]
36. Yang, H.; Zou, X.; Li, X.; You, R. Environmental data records from FengYun-3B Microwave Radiation Imager. *IEEE Trans. Geosci. Remote Sens.* **2012**, *50*, 4986–4993. [[CrossRef](#)]
37. Wolff, D.B.; Fisher, B.L. Assessing the relative performance of microwave-based satellite rain-rate retrievals using TRMM ground validation data. *J. Appl. Meteorol. Climatol.* **2009**, *48*, 1069–1099. [[CrossRef](#)]
38. Islam, T.; Rico-Ramirez, M.A.; Han, D.; Srivastava, P.K. Using S-band dual polarized radar for convective/stratiform rain indexing and the correspondence with AMSR-E GSFC profiling algorithm. *Adv. Space Res.* **2012**, *50*, 1383–1390. [[CrossRef](#)]
39. Iguchi, T.; Kozu, T.; Meneghini, R.; Awaka, J.; Okamoto, K.I. Rain-profiling algorithm for the TRMM precipitation radar. *J. Appl. Meteorol.* **2000**, *39*, 2038–2052. [[CrossRef](#)]
40. Shige, S.; Takayabu, Y.N.; Tao, W.K.; Shie, C.L. Spectral retrieval of latent heating profiles from TRMM PR data. Part II: Algorithm improvement and heating estimates over Tropical Ocean regions. *J. Appl. Meteorol. Climatol.* **2007**, *46*, 1098–1124. [[CrossRef](#)]
41. Seto, S.; Iguchi, T.; Utsumi, N.; Kiguchi, M.; Oki, T. Evaluation of extreme rain estimates in the TRMM/PR standard product version 7 using high-temporal-resolution rain gauge datasets over Japan. *SOLA* **2013**, *9*, 98–101. [[CrossRef](#)]
42. Kirstetter, P.-E.; Hong, Y.; Gourley, J.J.; Schwaller, M.; Petersen, W.; Zhang, J. Comparison of TRMM 2A25 products, version 6 and version 7, with NOAA/NSSL ground radar-based National Mosaic QPE. *J. Hydrometeorol.* **2013**, *14*, 661–669. [[CrossRef](#)]
43. Tu, J.Y.; Chou, C.; Chu, P.S. The abrupt shift of typhoon activity in the vicinity of taiwan and its association with western North Pacific-East Asian climate change. *J. Clim.* **2009**, *22*, 3617–3628. [[CrossRef](#)]
44. Shibata, A. A wind speed retrieval algorithm by combining 6 and 10 GHz data from Advanced Microwave Scanning Radiometer: Wind speed inside hurricanes. *J. Oceanogr.* **2006**, *62*, 351–359. [[CrossRef](#)]
45. Yin, X.; Wang, Z.; Song, Q.; Huang, Y.; Zhang, R. Estimate of ocean wind vectors inside tropical cyclones from polarimetric radiometer. *IEEE J. Sel. Top. Appl. Earth Obs. Remote Sens.* **2017**, *10*, 1701–1714. [[CrossRef](#)]
46. Wentz, F.J. A well-calibrated ocean algorithm for Special Sensor Microwave/Imager. *J. Geophys. Res. Oceans* **1997**, *102*, 8703–8718. [[CrossRef](#)]
47. Petković, V.; Kummerow, C.D. Understanding the sources of satellite passive microwave rainfall retrieval systematic errors over land. *J. Appl. Meteorol. Climatol.* **2017**, *56*, 597–614. [[CrossRef](#)]
48. Meissner, T.; Wentz, F.J. Wind-vector retrievals under rain with passive satellite microwave radiometers. *IEEE Trans. Geosci. Remote Sens.* **2009**, *47*, 3065–3083. [[CrossRef](#)]
49. Ulaby, F.T. *Microwave Remote Sensing Active and Passive-Volume III: From Theory to Applications*; Artech House: Dedham, MA, USA, 1986.
50. Houze, R.A., Jr. Clouds in tropical cyclones. *Mon. Weather Rev.* **2010**, *138*, 293–344. [[CrossRef](#)]

